Effect of angle of attack on the instability-wave selectivity in hypersonic compression ramp laminar flow

Qiushi Huang,[1] Chang Sun,[2] and Peixu Guo*[1]
[1)]*Department of Aeronautical and Aviation Engineering, The Hong Kong Polytechnic University, 11 Yuk Choi Road, Hong Kong SAR, China*
[2)]*Department of International Cooperation, Beijing Microelectronics Technology Institute, No.2, North Siyingmen Road, 100076 Beijing, China*

(*Electronic mail: peixu.guo@polyu.edu.hk)

(Dated: 4 December 2025)

This study investigates the effect of angle of attack (AOA) on the convective instability of a hypersonic flow over a compression ramp at Mach 7.7, with particular emphasis on high-frequency two-dimensional Mack modes and low-frequency three-dimensional shear-layer instabilities. Combining linear stability theory (LST) and resolvent analysis, we examine how the change in AOA affects the convective instability mechanisms associated with separation bubbles. Results show that as AOA decreases from zero to negative, the separation bubble elongates, leading to increased growth rates and spatial extent of higher-order Mack modes. The negative AOA also promotes the emergence of additional shear-layer instabilities within concave high-curvature regions near the aft portion of the bubble. In contrast, positive AOAs compress the separation bubble, suppress higher-order modes, and reduce both the number and growth rates of shear-layer instability modes. Notably, at large positive AOA, the separation bubble acts as a broadband perturbation amplifier in the vicinity of the separation point for high-frequency Mack modes. For both large positive or negative AOAs, the low-frequency shear layer modes are shown to be unsteady Görtler modes. A comparison between LST and resolvent analysis demonstrated good agreement, confirming that the parallel-flow assumption underlying LST remains largely valid across multiple AOAs. These results indicate that, despite the changing bubble morphology with AOA, LST remains a valid tool for stability studies of the shock wave/boundary layer interaction (laminar flow).

NOMENCLATURE

$\tilde{c}$	=	complex phase velocity, $\tilde{c} = \omega/\alpha$
f	=	physical frequency
K	=	streamline curvature
M	=	Mach number
p	=	pressure
Re	=	Reynolds number
T	=	temperature
(u,v,w)	=	velocity components in Cartesian coordinate system
(x,y,z)	=	Cartesian coordinates in streamwise, wall-normal and spanwise directions
α	=	complex streamwise wavenumber
β	=	spanwise wavenumber
(ξ,η,z)	=	orthogonal body-fitted coordinates
ϕ	=	vector of primitive variables
ρ	=	density
σ	=	local growth rate
ϕ	=	vector of primitive variables
ψ	=	vector of modal shape function for primitive variables
ω	=	angular frequency

Subscripts

∞	freestream quantity
w	wall quantity
r	real part of complex number, or reattachment position
i	imaginary part of complex number
0	initial position

Subscripts

$*$	dimensional quantity
$'$	fluctuating quantity

I. INTRODUCTION

The shock wave/boundary layer interaction (SWBLI) is a common phenomenon in supersonic and hypersonic flows. The presence of a shock can cause flow separation and intense unsteadiness[1]. The turbulent SWBLI is more extensively studied, while the transitional SWBLI and the instability of laminar SWBLI receives growing attention recently. The instability of laminar SWBLI is responsible for the transition to turbulence, and thus the instability is of great significance.

Previous experimental and numerical work has shown that a laminar separation bubble can support two distinct types of instabilities[2,3]. In the convectively unstable case, upstream disturbances are amplified while being advected downstream. Thus, the bubble acts as a noise amplifier, and the presence of upstream disturbances is necessary. In the absolutely unstable case, perturbations grow temporally without the need for upstream disturbances, which trigger self-sustained global oscillations. In this scenario, the bubble acts as an intrinsic oscillator. These instabilities and the resulting transition can cause loss of aerodynamic efficiency, noise generation, and unsteady loads that may endanger structural safety[4,5]. Their manifestation is highly sensitive to external conditions and geometric configurations. In practical engineering applications, an aircraft operates over a range of angles of attack (AOA)

rather than a fixed value due to varying flight conditions and altitude. As a result, the angle of attack should be considered, which may significantly affect the size, location and stability characteristics of laminar separation bubbles. Therefore, it is important to investigate how convective instability waves interact with separation bubbles under different AOAs.

Regarding the convective instability, recent wind-tunnel experiments[6,7] have demonstrated the significance of traveling waves. Two fundamental mechanisms have been identified in hypersonic shock wave-boundary layer interactions (SWBLI): Mack modes of acoustic nature and shear layer modes associated with separation bubbles. Mack modes originate from high-speed boundary layers, typically manifesting as high-frequency disturbances in the order of hundreds of kilohertz. In contrast, shear layer modes are observed as lower-frequency oscillations with tens of kilohertz[8–10]. Experimental investigations employing surface pressure sensors and high-speed schlieren imaging have confirmed the coexistence of these two instability mechanisms, highlighting their distinct frequency signatures and spatial characteristics[11–14]. In particular, the experiments of Butler & Laurence[6] revealed that the laminar separation bubble tends to amplify the low-frequency shear-layer modes and almost freeze the high-frequency Mack modes. In other words, for the separation bubble, there is a selection process for instability waves. The recent stability analyses by Guo et al.[15] have clarified the selectivity by clearly identifying the unstable regions and showing the instability nature.

Regarding the eigenmode, Mack modes are newly generated solutions in high-speed boundary layers, unlike the Tollmien–Schlichting (T–S) waves in subsonic cases. As the Mach number increases to around 4, multiple unstable Mack modes emerge within the boundary layer. Among them, the second mode generally exhibits the highest growth rate, which is thus considered the dominant factor leading to the linear instability of the boundary layer and thus its eventual transition. For SWBLI flows, linear stability theory (LST) suggests that high frequency two-dimensional (2D) Mack modes exhibit neutral oscillations within laminar separation bubbles and display complex modal synchronization behavior[15]. An excellent agreement was reached between the local LST and the global resolvent analysis in terms of both the growth rate and the mode shape. Here, the global resolvent analysis is based on the linearized Navier–Stokes (N–S) equation without further simplification . Thus, the resolvent analysis provides the "accurate" solution resembling a direct numerical simulation in the linear instability stage. A good agreement with the global resolvent analysis indicates that LST could provide a good estimate of flow instability in weakly separated flows. The rationale of the reliable locally parallel analysis in separated flows was also provided by Diwan and Ramesh[16]. Furthermore, it should be remembered that the terms "local" and "global" refer to the instability of a local flow profile and of the entire flow field, respectively[2].

As for shear layer modes, they were previously attributed to the Kelvin–Helmholtz (K–H) instability mechanism, which arises at fluid interfaces with significant velocity gradients. However, in hypersonic compression ramp flows, flow compressibility would suppress the K–H mode[17]. Our recent studies[15] revealed that this instability is more likely to originate from Görtler instability, with multiple Görtler modes distributed continuously along the streamwise direction. This feature collectively forms the amplification region of three-dimensional (3D) disturbances. Given the high sensitivity of Görtler instability to streamline curvature, further questions arise. As mentioned previously, since altering the angle of attack could modify the shape of the separation bubble, how does this result affect the streamline curvature? How might it influence the shear layer modes? Furthermore, does the change in separation bubble size affect the synchronization process of Mack modes? What types of Mack modes might emerge under different AOAs of the incoming flow?

To elucidate the amplification mechanisms of these instability modes under varying AOAs, this study employs LST and resolvent analysis. LST serves as a local method that relies on the parallel flow assumption, analyzing boundary layer stability at individual streamwise stations[2]. It provides a framework to quantify the spatial growth rates of instability waves, offering valuable predictions of local mode frequencies and amplification characteristics under different external conditions. In contrast, resolvent analysis constitutes a global approach that treats the entire spatially developing flow field as a unified system, fully accounting for non-parallel effects. This method identifies the most amplified convective modes or optimal forcing responses by solving an input–output problem, capturing how disturbances evolve and interact throughout the domain. As resolvent analysis provides a more complete representation of the linear system, it yields results that align more closely with actual physical behavior. This is particularly evident in flows with separation bubbles, which are considered highly non-parallel. To compare LST and resolvent analyses offers a valuable basis for evaluating the reliability of LST and reveals its possible limitations under different AOAs.

In our previous work[15], a comprehensive investigation into the instability-wave selectivity of a hypersonic compression ramp flow at AOA = 0° was conducted. The study employed a 12° compression ramp model under Mach 7.7 freestream conditions with a unit Reynolds number of 4.2×10^6 m^{-1}, combining resolvent analysis, LST, and parabolized stability equations (PSE) to examine the interaction between instability waves and the laminar separation bubble. The key finding was that the laminar separation bubble acts as a selective amplifier for convective instability waves. Specifically, for the 2D, high-frequency Mack modes, the separation bubble was found to support the emergence of multiple higher-order modes (up to the fifth order). These modes underwent a complex process of repeated modal synchronizations, creating alternating stable and unstable regions. These intricate dynamics resulted in a characteristic neutral oscillation of the disturbance energy within the bubble, manifesting as a streamwise "freezing" of its growth. In contrast, the bubble persistently amplifies 3D, low-frequency disturbances. These shear-layer modes were conclusively identified as unsteady Görtler modes, whose growth is primarily governed by the streamline curvature. Their continuous amplification results from the successive dominance of multiple local unstable

eigenmodes along the streamwise direction. Excellent agreement between LST and global resolvent analysis validated this eigenmodal interpretation of the selective amplification mechanism at AOA = 0°, establishing the baseline for the current study.

This study will primarily investigate the following questions:
1) How does the AOA affect the shape of the separation bubble and the curvature of nearby streamlines?
2) What characteristics do Mack modes exhibit under different AOAs?
3) How are shear-layer modes affected by the AOA?
4) Can LST still achieve good agreement with the resolvent analysis under different AOAs?

II. PROBLEM DESCRIPTIONS

To investigate the effects of the AOA on Mack and shear-layer modes, a compression corner configuration shown in Fig. 1 is adopted in this paper, which is consistent with our previous work[15]. The model is assumed to possess a sufficiently large width in the spanwise direction to neglect cross-flow effects. This treatment was also adopted by the numerical simulation of the laminar SWBLI with varying AOA by Khraibut & Gai[18]. It will be later shown that without involving the cross-flow effect, the flow physics are already complicated. The compression corner model consists of a flat plate section with a length of $L^* = 100$ mm, followed by an 80-mm ramp set at an angle of 12°. Here, the asterisk (*) denotes dimensional quantities. The freestream condition, following an experimental one[19], is set as follows: Mach number $M_\infty = 7.7$, unit Reynolds number $Re^*_\infty = 4.2\times10^6$ m^{-1}, and static temperature $T^*_\infty = 125$ K. A total of nine AOAs are considered, ranging from $-8°$ to $+8°$ with the 2° increments. Here, the AOA is defined as the angle between the vector of freestream velocity and the chord line of the flat plate section of the model. A positive AOA corresponds to the leading edge of the plate pitching upwards, which is equivalent to the freestream direction turning counterclockwise relative to the plate, while a negative AOA pitches the leading edge downwards.

In this paper, primitive variables are nondimensionalized using freestream reference values, except for the pressure p, which is nondimensionalized by $\rho^*_\infty u^{*2}_\infty$, where ρ denotes density. The reference length for nondimensionalization is equal to the plate length L^*. A Cartesian coordinate system (x,y) is defined with its origin at the leading edge; the corresponding velocity components are (u,v) in the x and y directions, respectively. An orthogonal body-fitted coordinate system (ξ,η) is also introduced, aligned with the wall-tangent and wall-normal directions. The wall temperature is maintained at a room temperature, $T^*_w = 293$ K, which is due to the short duration of the hypersonic experiment.

Consistent with the previous work[15], an in-house N–S solver is employed to obtain the laminar base flow. Freestream conditions are imposed on the left and upper boundaries of the computational domain, as illustrated in Fig. 1. The right boundary is treated with a simple extrapolation condition, while the model surface employs an isothermal no-slip condition. The mesh convergence has been examined and guaranteed for each simulated case in the present paper, as done in our previous work[15]. The current mesh resolution is 1200×350, which is deemed sufficient by comparing the baseflow and resolvent-analysis results to those obtained on a coarser mesh (1000×300).

It is noteworthy to address the stability regime of the base flows considered herein. Following the work of Hao et al.[20], the present configuration at AOA = 0° is known to exhibit convective instability without global (absolute) instability. However, the global stability analysis[20] (results not shown for brevity) confirms that as the AOA decreases to -6° and -8°, global instability emerges. While global instability signifies a temporal mechanism where perturbations grow in place over time, ultimately leading to self-sustained oscillations, the present LST and resolvent analyses are notably conducted on a strictly converged steady-state base flow. Consequently, this approach characterizes the linear dynamics of the unperturbed flow during the initial stages, prior to finite-amplitude oscillations dominating the system. Nonetheless, even as an approximation, this linear analysis still offers valuable insights into the underlying stability mechanisms for these extreme negative-AOA cases.

III. STABILITY ANALYSIS TOOLS

A. Linear Stability Theory (LST)

Linear Stability Theory is a classical tool in the study of convective instabilities. The derivation starts from superimposing small disturbances onto a known base flow and linearizing the N–S equation. A core assumption of LST is that the flow can be locally approximated as parallel. As a result, the linearized N–S equation can be transformed into an eigenvalue problem. Solving this problem yields the growth rates and propagation characteristics of the disturbances. Historically, the separation bubble was considered highly non-parallel. However, Diwan & Ramesh demonstrated the applicability of LST to separation bubbles through an investigation[16]. Sansica et al.[21] and Jaroslawski et al.[22] have also successfully applied LST to investigate separation bubbles, achieving consistent and promising results.

To be specific, the disturbance is assumed to take the form

$$\phi' = \psi(\xi,\eta)\exp(\mathrm{i}\alpha\xi + \mathrm{i}\beta z - \mathrm{i}\omega t) + \text{c.c.}, \tag{1}$$

where α and β are the wavenumbers in the streamwise and spanwise directions, respectively. The symbols z, t, ω and c.c. refer to the spanwise coordinate, the time, the circular frequency and the complex conjugate, respectively. The symbol $\psi = (\hat\rho,\hat u,\hat v,\hat w,\hat T)^{\mathrm{T}}$ is the shape function (eigenvector), where w is the spanwise velocity. The governing equation is written as

$$\mathscr{L}_0\psi = \mathbf{0}. \tag{2}$$

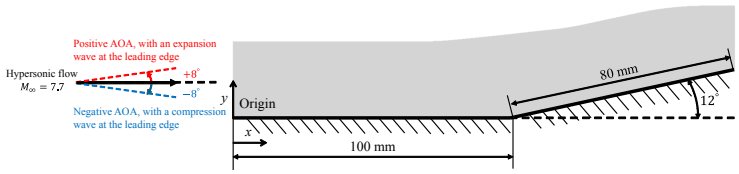

FIG. 1. Schematic of the flow configuration, with the gray region representing the computational domain.

Here, $\mathscr{L}_0$ is the linear operator for a parallel flow. In a body-fitted coordinate system, the equation can be rewritten as

$$\boldsymbol{H}_{yy}\frac{\partial^2\psi}{\partial\eta^2}+\boldsymbol{H}_y\frac{\partial\psi}{\partial\eta}+\boldsymbol{H}_0\psi=\boldsymbol{0}, \tag{3}$$

where $\boldsymbol{H}_{yy}$, $\boldsymbol{H}_y$, and $\boldsymbol{H}_0$ are matrices that depend on the base flow, wavenumbers α and β, and the metric factor h_1. Detailed expressions are found in the work of Ren & Fu[23]. The factor h_1 is defined as

$$h_1=1+K\eta, \tag{4}$$

where K denotes the streamline curvature. The value of h_1 is obtained by computing the full-field curvature $K(\xi,\eta)$. The boundary conditions are specified as follows:

$$\begin{cases}\hat{u}=\hat{v}=\hat{w}=\hat{T}=0, \eta=0\\ \hat{u}=\hat{v}=\hat{w}=\hat{T}=0, \eta\to\infty.\end{cases} \tag{5}$$

So far, the linear system reduces to an eigenvalue problem for α, where the imaginary part of α corresponds to the growth rate of a given mode, defined as $\sigma=-\alpha_i$. A mode is considered stable if $\alpha_i>0$, and unstable if $\alpha_i<0$. In this study, a hybrid numerical approach combining spectral and finite-difference methods was employed for LST analysis. The process began with the application of a Chebyshev spectral collocation method to directly obtain the complete stability spectrum. Subsequently, an iterative fourth-order compact difference scheme was introduced to refine the computation of eigenmodes, as this scheme exhibits significantly lower sensitivity to grid distribution compared to the spectral method. Specifically, the discrete eigenmodes obtained from the spectral method served as initial guesses for the iterative computations performed using the compact difference scheme. With a grid resolution of $N_y=220$ collocation points, the Euclidean norm of the difference in the eigenvalue α for the most unstable mode between the two methods remained below 0.5% across all AOAs, indicating excellent agreement and numerical accuracy. To optimize computational efficiency, a downstream marching step size of $\Delta x<0.004$ was employed for the 2D instability modes (to facilitate scanning the x–ω plane) and a finer step of $\Delta x<0.001$ for the 3D shear layer modes. The LST code has been well validated through comparisons with theoretical, numerical and experimental results[24–28].

B. Resolvent Analysis

Resolvent analysis can describe how the flow responds to external forcings. This method reveals linear amplification mechanisms of instabilities in the entire flow field, manifested by the relationship between input (exerted forcing) and output (flow response). The most amplified disturbance is found by analyzing the "resolvent operator". i.e., the transfer function that quantifies this amplification effect[29]. The corresponding linearized N–S equations are expressed as the matrix system

$$\partial\boldsymbol{q}'/\partial t=\boldsymbol{A}\boldsymbol{q}'+\boldsymbol{B}\boldsymbol{f}', \tag{6}$$

where $\boldsymbol{A}$ is the Jacobian matrix obtained by linearizing the system around the base flow, and $\boldsymbol{B}$ defines how the forcing term $\boldsymbol{f}'$ is introduced into the state equations—typically constraining it to act at localized positions. The disturbance variable $\boldsymbol{q}'$ takes the form

$$\boldsymbol{q}'(x,y,z,t)=\hat{\boldsymbol{q}}(x,y)\exp(\mathrm{i}\beta z-\mathrm{i}\omega t)+\text{c.c.}, \tag{7}$$

and the forcing term $\boldsymbol{f}'$ is expressed as

$$\boldsymbol{f}'(x,y,z,t)=\hat{\boldsymbol{f}}(x,y)\exp(\mathrm{i}\beta z-\mathrm{i}\omega t)+\text{c.c.}. \tag{8}$$

Substituting equations (7) and (8) into equation (6) yields

$$\hat{\boldsymbol{q}}=\boldsymbol{R}\boldsymbol{B}\hat{\boldsymbol{f}}, \tag{9}$$

with the resolvent operator defined as

$$\boldsymbol{R}=(-\mathrm{i}\omega\boldsymbol{I}-\boldsymbol{A})^{-1}, \tag{10}$$

where $\boldsymbol{I}$ is the identity matrix. Subsequently, resolvent analysis serves to identify the forcing $\hat{\boldsymbol{f}}$ and the corresponding response mode $\hat{\boldsymbol{q}}$ that produce the maximum gain at a given frequency ω, referred to as the optimal gain. This is achieved through the singular value decomposition (SVD). The optimal gain G is defined as

$$G^2(\beta,\omega)=\max_{\hat{\boldsymbol{f}}}\left\{\|\hat{\boldsymbol{q}}\|_E/\|\boldsymbol{B}\hat{\boldsymbol{f}}\|_E\right\}, \tag{11}$$

where $\|\cdot\|_E$ denotes the energy norm based on Chu's energy[30]. This optimization can be reformulated as an eigenvalue problem[20]:

$$\boldsymbol{B}^*\boldsymbol{M}^{-1}\boldsymbol{R}^*\boldsymbol{M}\boldsymbol{R}\boldsymbol{B}\hat{\boldsymbol{f}}=G^2\hat{\boldsymbol{f}}. \tag{12}$$

Here, $\boldsymbol{M}$ is the weight matrix used to compute Chu's energy[30], and † denotes complex conjugate transpose. The computational process commences by solving the eigenvalue problem for given parameters β and ω using the ARPACK library, where the resulting dominant eigenfunction defines the spatial shape of the optimal forcing $\hat{\boldsymbol{f}}$; subsequently, the corresponding optimal response is calculated directly via (9). This numerical process relies on the discretization of the system matrix $\boldsymbol{A}$. A modified Ducros shock sensor identifies discontinuities in the flow field. Then, the inviscid fluxes near these regions are computed using a modified StegerWarming scheme, while a second-order central scheme is applied in smooth regions and for viscous fluxes. This code has also been well validated[20,27].

TABLE I. Separation and reattachment points, and separation length at different AOAs. x_s represents the separation location, x_r represents the reattachment location, and L_s represents the separation length. All values are non-dimensionalized by the plate length L^*.

AOA	x_s	x_r	L_s
-8°	0.74609	1.16774	0.42165
-6°	0.75458	1.17147	0.41689
-4°	0.76731	1.17334	0.40603
-2°	0.78428	1.17334	0.38906
0°	0.80546	1.17160	0.36614
+2°	0.82809	1.16774	0.33965
+4°	0.85239	1.16213	0.30974
+6°	0.88156	1.15465	0.27309
+8°	0.91478	1.14528	0.23050

IV. RESULTS

A. Variations in separation bubble structure and streamline curvature

In a 2D compression corner configuration, the inclined ramp introduces an adverse pressure gradient into the incoming flow. As the ramp angle increases, the flow within the boundary layer progressively decelerates. Once the adverse pressure gradient becomes sufficiently strong, a recirculation region develops near the wall, forming a separation bubble at the corner. Geometric parameters of the compression corner, such as the ramp angle, leading-edge bluntness and corner curvature, directly govern the strength and distribution of the adverse pressure gradient, thereby affecting the separation bubble.

Among these factors, the ramp angle most directly influences flow separation. In theory, it functions as a global parameter that can be systematically varied to affect the overall flow field. Specifically, an increase in the ramp angle intensifies the adverse pressure gradient, which promotes boundary layer separation and results in a larger and more pronounced separation bubble. Building on this understanding of the ramp angle as a governing parameter, a pivotal question emerges: can variations in the AOA serve as a similar, system-level influential parameter to produce analogous effects on the flow field?

As mentioned in Sec. II, this study considers nine cases with different AOAs. Fig. 2 and Fig. 3 present streamline and pressure contour plots in the left column, and curvature distributions above the dividing streamline in the right column. Using the AOA = 0° case as the baseline, the flow separation and reattachment locations are determined based on the surface skin-friction coefficient C_f, with the corresponding C_f distribution shown in Fig. 4.

As the AOA decreases, the adverse pressure gradient in Fig. 2 increases, causing the separation point to shift upstream (from $x_s = 0.805$ to $x_s = 0.746$), while the reattachment point remains relatively unchanged near $x_r = 1.171$. In contrast, as the AOA increases, the adverse pressure gradient in Fig. 3 is weakened, shifting the separation point downstream to $x_s = 0.915$ and the reattachment point upstream to $x_r = 1.145$. The specific separation and reattachment locations for all AOAs are summarized in Table I.

In compression corner flows, the separation bubble can be regarded as a "virtual wall" that forces the external streamlines to bend. Inside the bubble, fluid recirculates, causing the streamlines to form S-shaped curves or even closed loops[31]. At the separation and reattachment shocks, streamlines undergo abrupt deflections, resulting in regions of intense local curvature[32]. This phenomenon is clearly observed in the present cases, as shown on the right subfigures of Fig. 2 and Fig. 3.

Using the compression ramp at AOA = 0°, i.e. Fig. 2(*a*) and Fig. 2(*b*) as the reference, the depression of the separation bubble near the reattachment region and the three main high-curvature regions along its upper surface can be clearly identified. As the AOA decreases, the reattachment region exhibits increasingly pronounced concave curvature fields, while the front portion of the bubble's upper surface becomes notably flatter (see the deformation of the grey region on the right subfigures of Fig. 2).

To quantitatively assess the shock strength variations underlying these curvature changes, Fig. 5 presents numerical schlieren images visualizing the magnitude of the density gradient ($|\nabla\rho|$) for all AOAs. All images employ an identical and consistent grayscale mapping, where brighter intensities correspond to higher values of $|\nabla\rho|$, highlighting regions of strong density variations such as shock waves and shear layers. At AOA = 0°, the schlieren image reveals a well-defined separation shock emanating from the separation point, followed by a relatively uniform shear layer extending toward the reattachment region. As the AOA decreases to negative values, the separation shock intensifies significantly, evident from the increased brightness and sharper definition of the shock front. This stronger shock causes the streamline curvature in the corresponding region in the right subfigures of Fig. 2 to become more localized. Concurrently, the overall magnitude of $|K|$ in the reattachment region increases, with more frequent and widely spaced intervals of high curvature emerging gradually. This enhanced curvature in the reattachment region is primarily linked to the progressively deepening concavity observed on the aft upper surface of the separation bubble. Within this concave zone, subtle but persistent flow

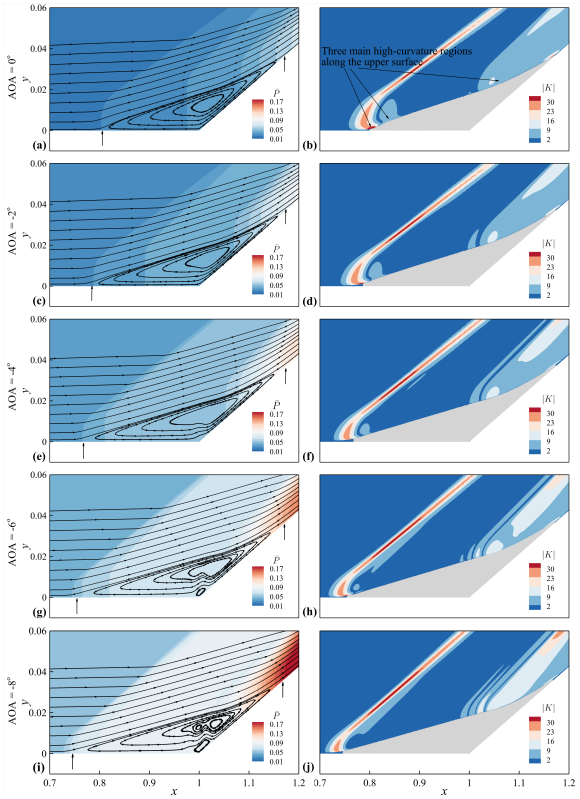

FIG. 2. All the cases at non-positive AOAs, the left column displays streamlines and pressure contours, while the right column shows the corresponding streamline curvature distributions $|K|$. The small arrows in the left column indicate the locations of flow separation and reattachment.

deflections generate a series of shock waves. These shocks, visually evident in the AOA = -6° and AOA = -8° images of Fig. 5, act to localize the streamline curvature within their immediate vicinity, thereby contributing to the discrete high-curvature intervals in Fig. 2(*h*) and Fig. 2(*j*).

Furthermore, at AOA = 0°, high-curvature regions are mainly concentrated near the separation point in Fig. 2(*b*). A subsequent slightly convex segment at around $x = 0.84$ in Fig. 2(*a*) also contributes to elevated local curvature. However, as the front portion of the separation bubble flattens, the high-curvature region around the separation point contracts. Concurrently, the high-curvature zone along the separation shock elongates from Fig. 2(*b*) to Fig. 2(*j*), while both the intensity and spatial extent of the curvature at the originally convex location at around $x = 0.84$ in Fig. 2(*b*) gradually diminish.

In Fig. 3, as the AOA increases, the front portion of the bubble's upper surface becomes more convex, leading to an augmentation in both the intensity and spatial extent of the high-curvature region between the separation and reattachment points. Owing to the blunter front of the separation bubble, the high-curvature zone near the separation point progressively widens. Meanwhile, as shown in Fig. 5, the separation shock weakens and becomes more diffuse with increasing AOA, resulting in reduced shock-induced curvature effects. Furthermore, from AOA = 0° to +8°, the reduced shear layer length causes the three originally distinct high-curvature regions visible at $x = 0.8$, $x = 0.84$, and $x = 1.05$ in Fig. 3(*b*) to move closer together. This process progressively compresses the dark blue low-curvature interval on the bubble's upper surface.

In summary, as the AOA decreases, the separation bubble is "stretched", leading to an enlarged recirculation zone and increased shear layer length. The high-curvature regions become concentrated primarily near the separation and reattachment points. Conversely, as the AOA increases, the separation bubble is "compressed", the recirculation zone shrinks,

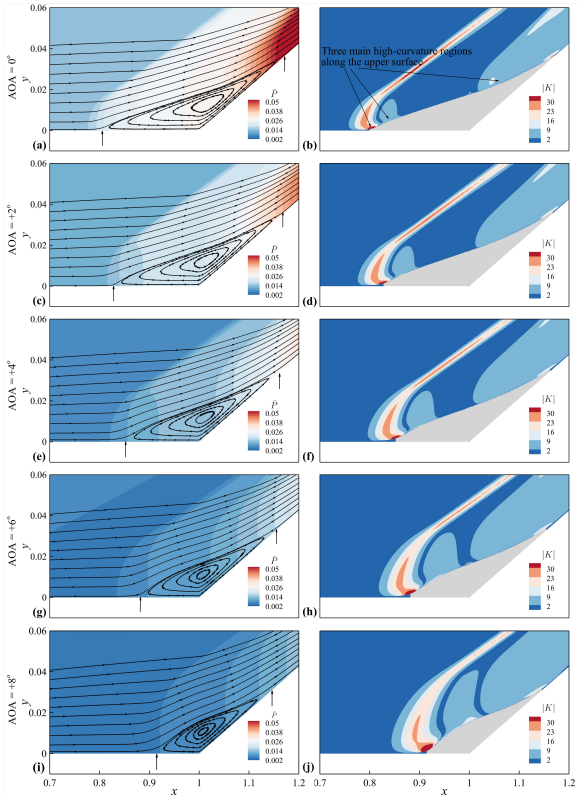

FIG. 3. All the cases at non-negative AOAs, the left column displays streamlines and pressure contours, while the right column shows the corresponding streamline curvature distributions $|K|$. The small arrows in the left column indicate the locations of flow separation and reattachment.

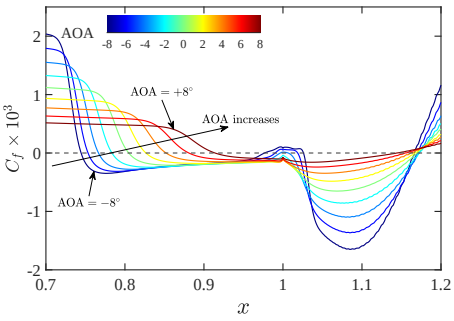

FIG. 4. Surface skin friction coefficient under all AOAs. x is non-dimensionalized by the plate length L^*.

and the front of the separation bubble exhibits a more convex morphology. This results in an extension of high-curvature regions across the streamline and progressive compression of the dark blue low-curvature interval on the upper surface of the separation bubble.

B. Effect of angle of attack on Mack modes

Unless otherwise stated, the results of planar waves ($\beta = 0$) are depicted, as they represent the most unstable scenario for Mack modes and are easier to investigate. Three-dimensional effects will be addressed later for shear-layer instabilities. Mack modes usually possess relatively high frequencies, typically with hundreds of kilohertz. In this study, the dimensionless angular frequency $\omega = 100$ corresponds to a dimensional frequency $f^* \approx 274.7$ kHz. To visually illustrate the Mack modes, the growth rate σ obtained from LST is plotted as a

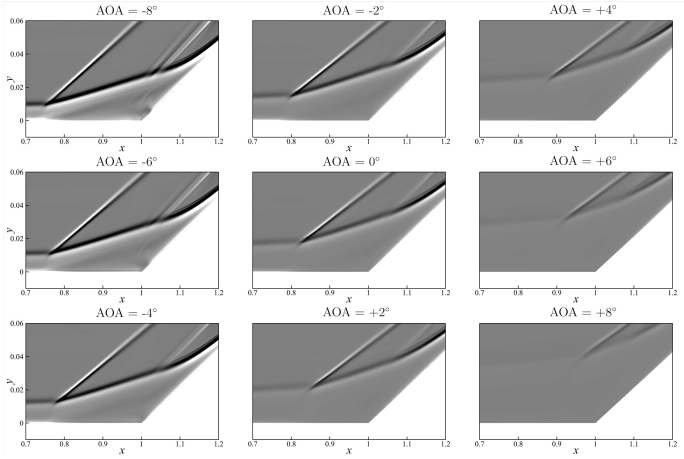

FIG. 5. Numerical schlieren images at all AOAs, showing the magnitude of the density gradient ($|\nabla\rho|$). A consistent grayscale is used for all images to facilitate comparison.

contour map against the streamwise position x and frequency ω. Contour maps for different AOAs are summarized in Fig. 6 and Fig. 7, where dashed lines indicate the locations of separation and reattachment points. Non-blue colored regions represent unstable local states. The color bar is set to a limited range of [1, 5] to optimally visualize the key features of the instability, as this specific range most clearly distinguishes the growth rates and spatial extents of various Mack modes. It can be observed that at zero and negative AOAs, the contours exhibit multiple inverted cone-like patterns, a configuration also reported in previous numerical simulation[33]. To highlight the influence of streamline curvature, the right columns of Fig. 6 and Fig. 7 show the corresponding results computed without curvature effects. This is done by taking the curvature $K = 0$ in LST.

Taking the case of AOA = 0° as a reference, when flow separation occurs, Mack modes of orders 2 to 5 are observed. The previous work[15] has shown that the unstable Mack's first mode is not present due to the high Mach number and cold wall condition. Thus, the lowest frequency of the unstable region corresponds to Mack's second mode. Notably, multiple modes of different orders can coexist at the same location, while a perturbation at a fixed frequency may undergo several distinct instability modes as it propagates streamwise. For instance, at a fixed frequency $\omega = 80$, the disturbance first experiences a second-mode instability, followed by alternating regions of stability and third-mode instabilities, before finally encountering another branch of the second-mode instability. This alternating sequence of unstable and stable regions results in a neutrally oscillating amplification of disturbances within the separation bubble. In our previous work[15], the neutral behavior of high-frequency Mack modes inside the separation bubble has been attributed to a complicated mode synchronization process triggered by flow separation. This process leads to streamwise-alternating zones of stability and instability, causing repeated growth and decay of disturbance energy. The separation bubble can thus be viewed as a complex "resonator" that facilitates the emergence of higher-order Mack modes. Given this mechanism, and since changes in AOA alter the size and shape of the separation bubble, a question arises: how exactly does AOA affect the Mack modes?

In Fig. 6, as the AOA decreases, the growth rate and spatial extent of higher-order modes gradually increase. This is likely associated with the increasingly elongated separation bubble. A larger and longer separation bubble provides a more extended development path for unstable waves, allowing them to accumulate more energy and reach higher amplitudes[34]. This observation aligns with the findings in low-speed flows regarding laminar separation bubbles, where longer bubbles exert a more significant global impact and support stronger instabilities compared to shorter ones[35]. In Fig. 7, as the AOA increases from zero, higher-order Mack modes are noticeably suppressed. This effect is more pronounced when streamline curvature is neglected. In the case of AOA = +8° (Fig. 7(*j*)), only two unstable modes remain. This suggests that the size of the separation bubble acts as a spatial filter, influencing the number of mode orders that can be sustained. Higher-order modes typically have shorter wavelengths and more complex spatial structures. A smaller separation bubble may be unable to accommodate the full waveform of these modes due to spatial constraints, or it may lack sufficient energy to excite them[36]. From the perspective of mode synchronization, a smaller separation bubble might not provide enough physical space to support repeated mode synchronization events. As a result, higher-order modes, which require longer evolution paths, disappear first.

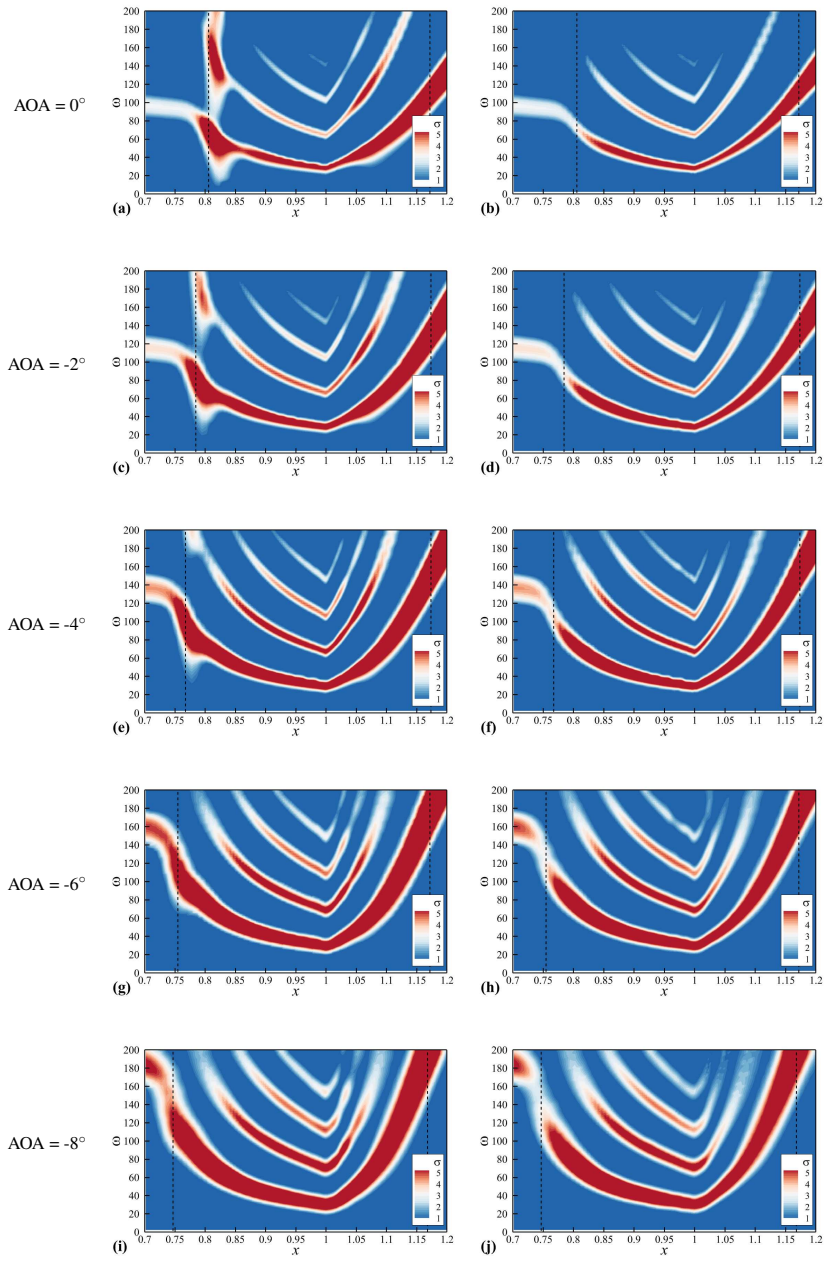

FIG. 6. Growth rate contours of the most unstable modes on the x–ω plane for all cases at non-positive AOAs, with the effects of streamline curvature involved in the left column but not in the right. The black dashed lines represent flow separation and reattachment. The AOA = 0° case is reproduced from the work by Guo et al.[15] as the baseline.

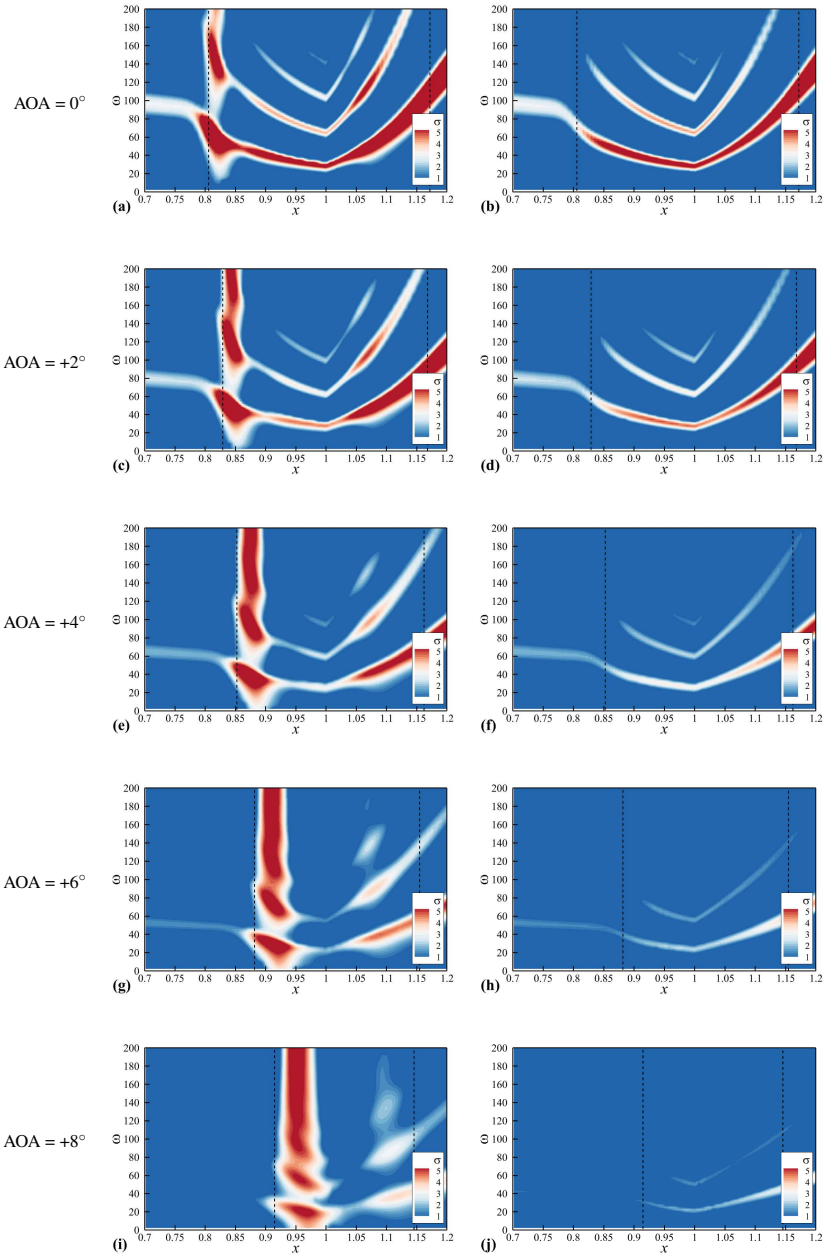

FIG. 7. Growth rate contours of the most unstable modes on the x–ω plane for all cases at non-negative AOAs, with the effects of streamline curvature involved in the left column but not in the right. The black dashed lines represent flow separation and reattachment. The AOA = 0° case is reproduced from the work by Guo et al.[15] as the baseline.

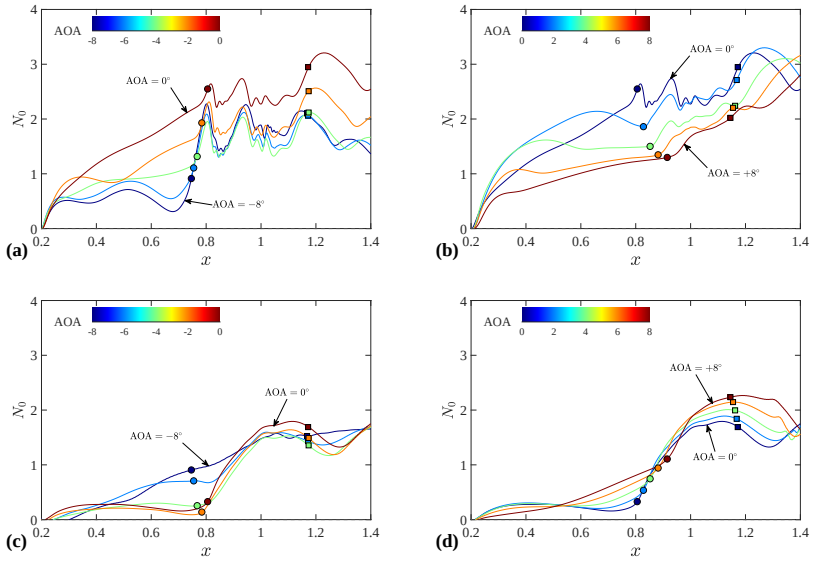

FIG. 8. N_0-factor curves of optimal disturbances using $x_0 = 0.2$ for (a) $\omega = 100$ under all non-positive AOAs, (b) $\omega = 100$ under all non-negative AOAs, (c) $\omega = 20$ under all non-positive AOAs, and (d) $\omega = 20$ under all non-negative AOAs. The separation and reattachment points are marked by solid circles and solid squares, respectively, with their colors matching the corresponding curve.

Additionally, Figs. 6 and 7 highlight the role of streamline curvature. At AOA = 0°, the centrifugal effect induced by high curvature near the separation and reattachment points enhances local instability. As the AOA decreases, the redistribution of high-curvature zones, as discussed earlier, weakens this enhancing effect. When the AOA decreases to -8°, the difference in the contour maps with and without curvature effects becomes less pronounced. In contrast, a growing AOA significantly amplifies the instability near the separation and reattachment points. As the AOA increases, the region of maximum curvature becomes growingly concentrated around the separation point, leading to gradual augmentation in both the magnitude and spatial extent of positive growth rates. By AOA = +8° (Fig. 7(i)), the unstable region near the separation point spans nearly all frequencies from low to high, forming a vertical band that acts as a broadband perturbation amplifier. This is an interesting finding that has not been reported before.

Previous studies have indicated that separation bubbles tend to selectively amplify 3D low-frequency disturbances, while "freezing" 2D high-frequency Mack-mode perturbations[15]. To further investigate how the variation in AOA and the associated alteration in separation bubble morphology affect this selection mechanism, resolvent analysis is employed to examine the evolution of perturbations. The input forcing is introduced at $x_0 = 0.2$, located far upstream of the separation point. To quantify the development of unstable disturbances, an N-factor is defined as

$$N_0 = 0.5 \ln \left(E_{\mathrm{Chu}} / E_{\mathrm{Chu},0} \right), \tag{13}$$

where E_{Chu} denotes Chu's energy density integrated from the wall to infinity in the η-direction, and $E_{\mathrm{Chu},0}$ is its value at the reference position $x_0 = 0.2$.

As demonstrated in the work of Guo et al.[15], at AOA = 0° the separation bubble exhibits a "freezing" effect on 2D disturbances at a frequency of $\omega = 100$. Specifically, the perturbation growth rate oscillates repeatedly within the separation bubble, resulting in an overall neutral behavior, i.e., neither significant growth nor decay. This trend is consistent with the streamwise evolution of the growth rate for fixed-frequency perturbations shown in Fig. 6(a). Further investigation with the 2D disturbance at $\omega = 100$ reveals that as the AOA gradually decreases from 0°, all negative AOAs exhibit similar oscillatory behavior within the separation bubble, as shown in Fig. 8(a). However, in Fig. 8(b), as the AOA increases from 0°, the amplitude of the oscillations gradually diminishes. By AOA = +8°, the N_0 factor exhibits a nearly monotonic increasing trend. Fig. 9 presents the 2D pressure fluctuations at $\omega = 100$. The black solid lines represent the isoline of the base pressure, drawn to visualize the separation shock, while the green curves indicate the dividing streamline. At AOA = 0°, the classical double-cell structure of Mack second mode is observed. The number of cells increases as AOA decreases. Conversely, as AOA increases, the number of cells

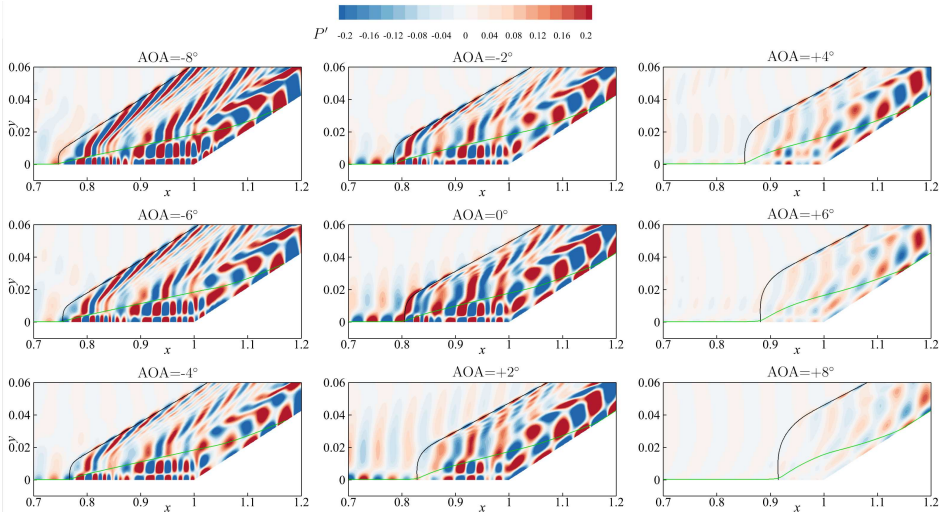

FIG. 9. Pressure fluctuations of the optimal disturbance with $\omega = 100$ for all AOAs as obtained by resolvent analysis. Black solid lines represent isolines of the base pressure, drawn to illustrate the separation shock. The isovalue of the black line is chosen such that it intersects with the wall at the separation point. Green curves indicate dividing streamlines.

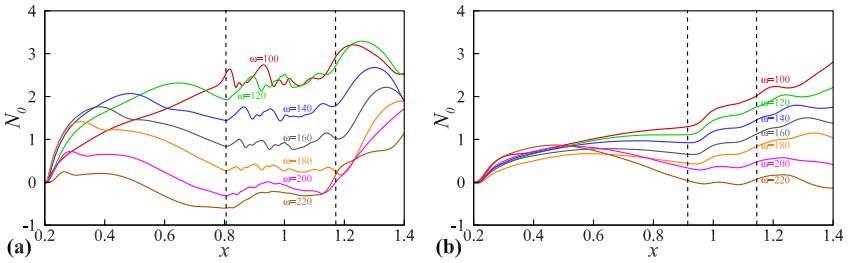

FIG. 10. N_0-factor curves based on $x_0 = 0.2$ of optimal disturbances for (a) AOA = 0° under different higher frequencies and (b) AOA=+8° under different higher frequencies. The black dashed lines represent flow separation and reattachment.

decreases significantly, indicating an attenuation of the separation bubble on pressure disturbances.

C. Selectivity of separation bubbles to high- and low-frequency 2D disturbances

A 2D disturbance with a frequency of $\omega = 20$ is employed to investigate the development of low-frequency perturbations within the separation bubble. Fig. 8(c) shows the energy development for all non-positive AOAs, which differs significantly from the high-frequency disturbance case in Fig. 8(a). Instead of exhibiting pronounced oscillations of curves, the disturbance energy tends to be constantly amplified by the separation bubble. Similarly, for all non-negative AOAs in Fig. 8(d), the energy also demonstrates a consistently growing trend. However, as the AOA increases from 0°, the difference in energy development behavior between the low-frequency case in Fig. 8(d) and the high-frequency case in Fig. 8(b) gradually diminishes. For instance, at AOA = +2°, the low-frequency disturbance in Fig. 8(d) exhibits nearly sustained growth within the separation bubble, whereas the high-frequency disturbance in Fig. 8(b) still shows clear oscillatory behavior. When the AOA increases to +8°, the curves for both the high and low frequencies in Fig. 8(b) and Fig. 8(d) exhibit a nearly monotonic increasing trend. Therefore, it can be concluded that at AOA = 0°, within a certain frequency range, the separation bubble exhibits distinct frequency-selective behav-

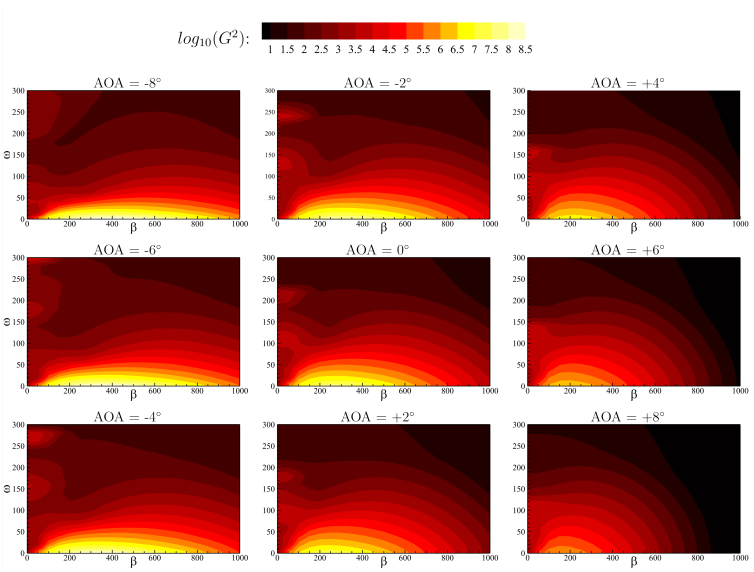

FIG. 11. Optimal gain under different AOAs by resolvent analysis.

ior. Specifically, it causes high-frequency perturbation amplitudes to oscillate while allowing low-frequency perturbations to undergo nearly sustained growth. This selection characteristic persists as the AOA decreases from 0°. In contrast, as the AOA increases from 0°, this frequency selection gradually diminishes.

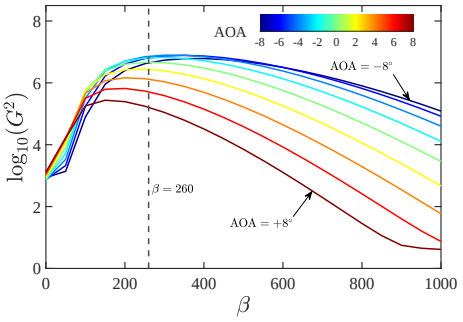

FIG. 12. Optimal gain under different AOAs with $\omega = 20$.

It is noteworthy that at a fixed AOA = +8°, as shown in Fig. 10(*b*), the energy growth of all high-frequency disturbances within the separation bubble exhibits a "increase-freezing-increase" three-stage feature. This pattern markedly differs from the AOA = 0° baseline case in Fig. 10(*a*), where the curves show repeated oscillations and lack a broad consistency in their evolutionary trends across all studied high-frequency perturbations in the separation bubble. This consistent energy evolution trend in Fig. 10(*b*) can be explained by the growth-rate variation in Mack modes under growing positive AOAs, as depicted in Fig. 7. Taking the curvature-included case at AOA = +8° in Fig. 7(*i*) as an example, high-frequency disturbances ($\omega > 100$) propagating in the streamwise direction generally experience three distinct intervals: an initial unstable region, a stable region, and then another unstable region—closely matching the three-stage evolution of the N_0-factor inside the separation bubble shown in Fig. 10(*b*).

Furthermore, in the previous study[15], the eigenfunctions and disturbance profiles obtained using the local method (LST) and the global method (resolvent analysis) at AOA = 0° were compared and showed good agreement. For brevity, a comparison of Mack mode disturbance shapes at other AOAs is not presented here, as this study focuses more on the 3D shear layer mode.

D. Effect of AOA on shear layer modes

Similar to 2D high-frequency disturbances, 3D low-frequency disturbances with tens of kilohertz also exhibit multimodal characteristics. The "multimodal" is manifested as multiple unstable modes appearing at the same streamwise location. These successively emerging unstable modes each become the dominant (most unstable) mode at different posi-

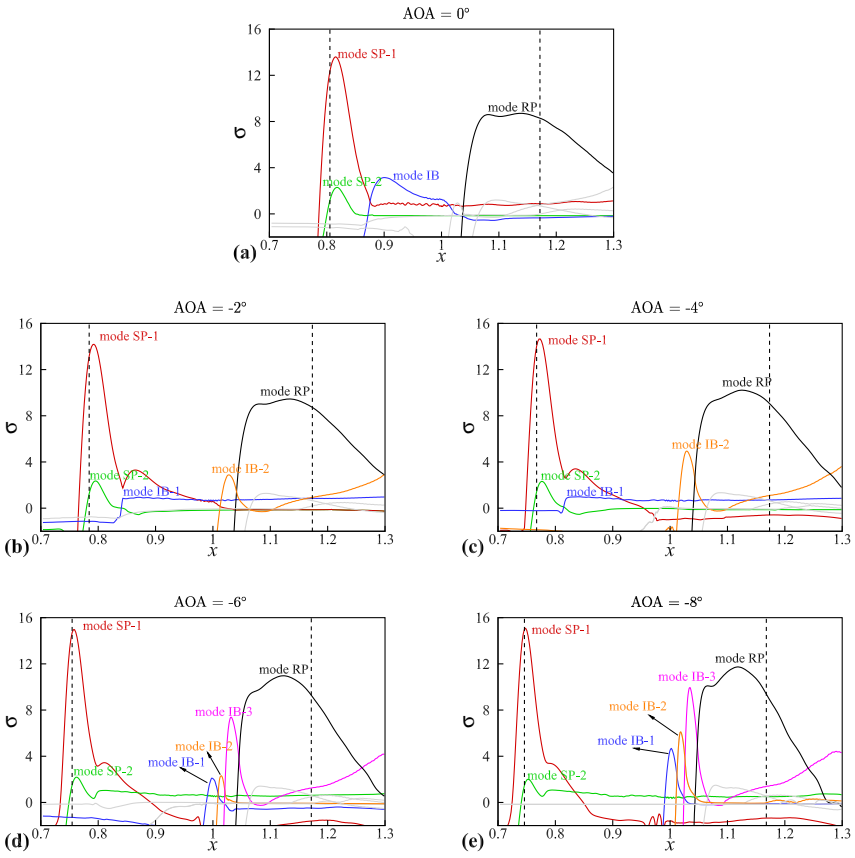

FIG. 13. Growth rates of unstable modes for non-positive AOA cases, from 0° to -8°. The black dashed lines represent flow separation and reattachment.

tions. The behavior collectively forms a continuous amplification region for low-frequency disturbances.

Before further discussing the characteristics of unstable modes at various AOAs, Fig. 11 presents the optimal gain obtained through resolvent analysis as a function of frequency ω and spanwise wavenumber β. It is important to note that this optimal gain quantifies the global energy amplification of the output response subject to the input forcing, and the output is not evaluated at a specific outflow location. The input forcing is spatially localized at the inflow position $x_0 = 0.2$, while the output is measured by the Chu's energy integrated over the entire computational domain. This approach captures the maximum energy growth from the localized forcing to the global flow response, ensuring that the gain reflects the system's overall amplification characteristics without dependence on a single downstream station. As shown in Fig. 11, the most amplified disturbances are concentrated in the low-frequency range and exhibit clear dependence on the spanwise wavenumber. The observation indicates that the separation bubble preferentially amplifies 3D low-frequency disturbances for nearly all AOAs. Taking AOA = 0° as the reference case, as AOA gradually decreases, the region with high gain values is extended toward both lower and higher spanwise wavenumbers. In other words, wider spanwise scales are involved and amplified by the separation bubble. In comparison, as AOA increases, this region contracts and shifts overall toward lower wavenumbers, suggesting smaller spanwise scales selected. For example, in Fig. 12, at a fixed disturbance frequency of $\omega = 20$, the wavenumber corresponding to the maximum gain is reduced with an increasing AOA. Mean-

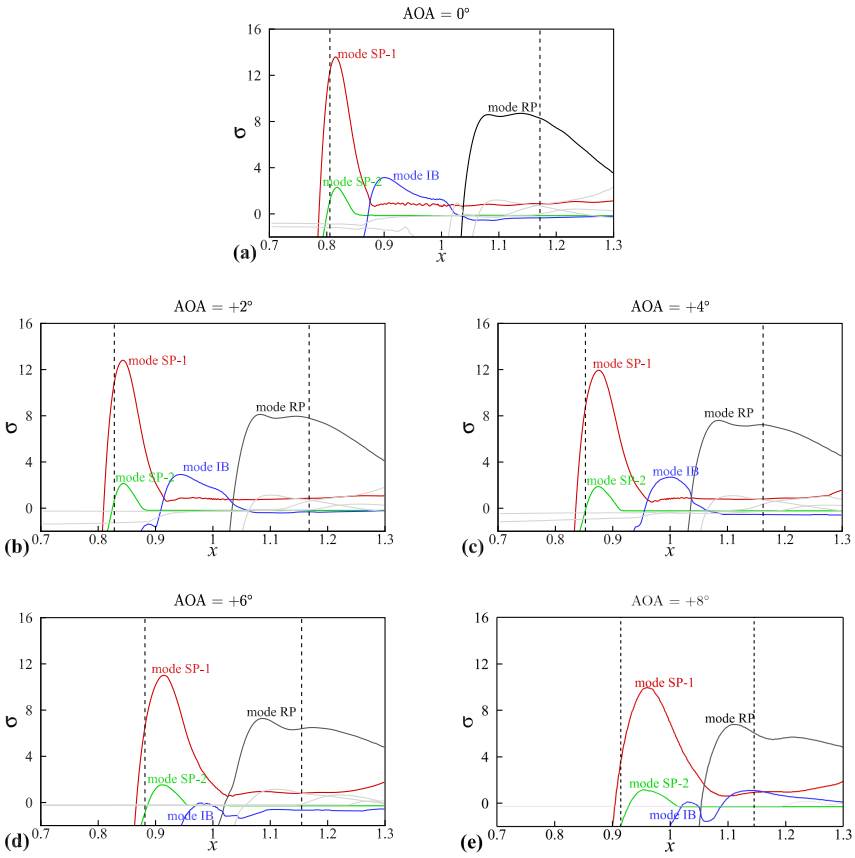

FIG. 14. Growth rates of unstable modes for non-negative AOA cases, from 0° to +8°. The black dashed lines represent flow separation and reattachment.

while, the range of wavenumbers spanning the same gain is gradually narrowed.

This study focuses on the 3D low-frequency mode characterized by a frequency $\omega = 20$ and a spanwise wavenumber $\beta = 260$. This selected pair corresponds to the peak gain at this low frequency under zero AOA. To clearly distinguish between individual modes, the following naming convention is adopted: the mode closest to the separation point is denoted as SP, the mode within the separation bubble as IB, and the mode near the reattachment point as RP.

Fig. 13 and Fig. 14 depict all unstable modes tracked across various AOAs. The more prominent unstable modes are highlighted with colored curves and labels, while others are displayed using gray curves. The complex velocity $\tilde{c} = \omega/\alpha$ is introduced, and $\tilde{c}_r$ and $\tilde{c}_i$ represent the real and imaginary parts of the modes, respectively. Each mode is tracked along the streamwise direction using a grid spacing $\Delta x < 0.001$. The tracking criterion relies on the minimal change in the complex velocity $\tilde{c}$ for the same mode between adjacent streamwise positions. Specifically, among all candidate modes at x_{i+1} with mode index j, the successfully traced mode minimizes the Euclidean norm $||\tilde{c}(x_i) - \tilde{c}_j(x_{i+1})||$.

We first analyze Fig. 13(*a*), which displays the variation of growth rate along the streamwise direction at AOA = 0°. As flow separation initiates, the mode SP-1 emerges near the separation point. The mode SP-2 also arises within the unstable region associated with mode SP-1, albeit with a notably lower growth rate. Mode IB develops inside the separation bubble, reaching its peak growth rate at around $x = 0.9$. At this location, mode IB coexists with mode SP-1. Subsequently, mode

RP forms in the vicinity of the reattachment point, accompanied by three other less prominent modes. In the corresponding complex-plane trajectory shown in Fig. 20(*a*), modes SP-1, IB, and RP independently evolve from very stable discrete modes, which appear successively on the stable half-plane of the complex phase velocity. The modes SP-1, IB, and RP each dominate distinct streamwise regions, constituting a continuous amplification zone for disturbances. It is noteworthy that these three modes are observed across all AOAs, indicating that they represent inherent characteristics generated by flow separation and reattachment in the present configuration.

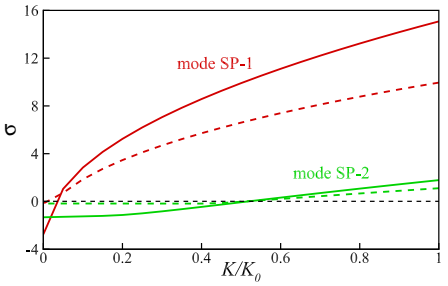

FIG. 15. The local growth rate versus the curvature ratio K/K_0 for modes SP-1 and SP-2 ($\omega = 20$, $\beta = 260$). The solid and dashed lines correspond to AOA = -8° ($x = 0.7461$) and AOA = $+8^\circ$ ($x = 0.9596$), respectively. Here, K_0 represents the actual local curvature, and the prefix "SP" indicates that these modes are located near the separation point.

As the AOA decreases from zero, the most significant changes occur in the original modes SP-1 and IB. In Fig. 13(*b*) at AOA $= -2^\circ$, the growth rate of mode SP-1 reaches its maximum at around $x = 0.8$ and then decays rapidly. Following that, a brief resurgence occurs near $x = 0.84$, after which it decays again toward zero. It is important to note that this resurgence of SP-1 is not an isolated event but occurs in the context of its synchronization with the emerging IB-1 mode. With their real phase velocities closely matched (SP-1: $\tilde{c}_r = 0.9103$, IB-1: $\tilde{c}_r = 0.9515$ at $x = 0.84$, see Fig. 20(*b*)), the condition for modal orthogonality breaks down, leading to a notable inter-modal interaction. This interaction may facilitate a temporary energy exchange, manifesting as the observed recovery in SP-1's growth rate. Correspondingly, the trajectory of SP-1 forms a distinct loop in the complex plane where its imaginary part $\tilde{c}_i$ ceases descending and rises again near $\tilde{c}_r = 0.91$, coinciding with this temporary increase in growth rate. Around $x = 0.84$, a new unstable mode IB-1 is observed, which originates from the entropy/vorticity continuous spectrum (a reservoir of neutral background disturbances inherent to the base flow) and exhibits a rapid increase in growth rate after $x = 0.83$. Furthermore, the growth rate of mode IB-2 increases sharply within a high curvature interval near $x = 1$ in Fig. 2(*d*). Next, as shown in Fig. 13(*b*), mode IB-2 decays, before rising slowly again after $x = 1.08$. Its trajectory in the complex plane shown in Fig. 20(*b*) exhibits a distinct V-shaped pattern.

As AOA is further decreased to -6° in Fig. 13(*d*), three unstable modes denoted IB-1, IB-2, and IB-3 are observed in the vicinity of x=1 in the bubble. Their unstable regions align closely with the three short spike-like high-curvature intervals near $x = 1$ in Fig. 2(*h*). The increasing amplitude of modes at decreased AOAs (enhanced curvature) supports the hypothesis that these disturbances in the tens of kilohertz range are most likely amplified by a Görtler-mode instability, which is highly sensitive to curvature[19]. This behavior becomes even more evident in Fig. 13(*e*). Not only do the locations of IB-1, IB-2, and IB-3 correspond to the three high curvature regions in Fig. 2(*j*), but their growth rates are also enhanced due to the stronger centrifugal effect. This stronger centrifugal effect results from the more concave aft portion of the separation bubble. In contrast, within the interval from $x = 0.8$ to $x = 0.98$ in both Fig. 13(*d*) and Fig. 13(*e*), the surface of the separation bubble remains relatively flat and the streamline curvature is uniform. As a result, no new unstable modes emerge in this region.

As the angle of attack increases from zero in Fig. 14, the maximum growth rates of all unstable modes gradually decrease. This finding is consistent with the variation in the gain by resolvent analysis, as shown in Fig. 12. As the separation bubble becomes more compressed, its upper surface slightly bulges, resulting in three relatively extensive high-curvature regions. Near the front of the separation bubble, the streamwise extent dominated by modes SP-1 and SP-2 widens with an increasing AOA. Close to the reattachment point, mode RP remains dominant throughout. However, between the separation and reattachment points, both the maximum growth rate and the dominant region of mode IB diminish. For example, in Fig. 14(*a*), mode IB dominates the unstable region from $x = 0.87$ to $x = 1.01$, whereas in Fig. 14(*c*), this interval narrows to between $x = 0.96$ to $x = 1.03$. In Fig. 14(*d*) and Fig. 14(*e*), the maximum growth rate of mode IB is even lower than that of mode SP-1 across the entire separation bubble. Moreover, in Fig. 14(*e*), mode IB emerges at $x = 1$ and reaches a minor local peak in growth rate at $x = 1.03$. It then decays briefly, rises again at $x = 1.06$, and attains its maximum growth rate at $x = 1.14$ before gradually decaying further. Thus, this in-bubble mode is becoming less and less significant as the bubble shrinks with an increasing AOA.

Another observation inside the bubble is that, from AOA = 0° to AOA = $+8^\circ$, no new IB modes are observed. This is likely due to the combination of two factors: 1) the relatively broad and smoothly varying high-curvature region in the middle of the separation bubble, where no abrupt curvature change occurs, and 2) the further reduced size of the bubble, which may limit the spatial development of additional modes.

Furthermore, previous studies have confirmed that at a freestream Mach number 7.7 and AOA = 0°, the origin of these unstable shear layer modes is related to unsteady Görtler-mode instabilities. These Görtler modes are particularly sensitive to streamline curvature[15]. Across the nine cases considered in this study, the unstable shear layer modes continue to exhibit a strong dependence on curvature as the AOA

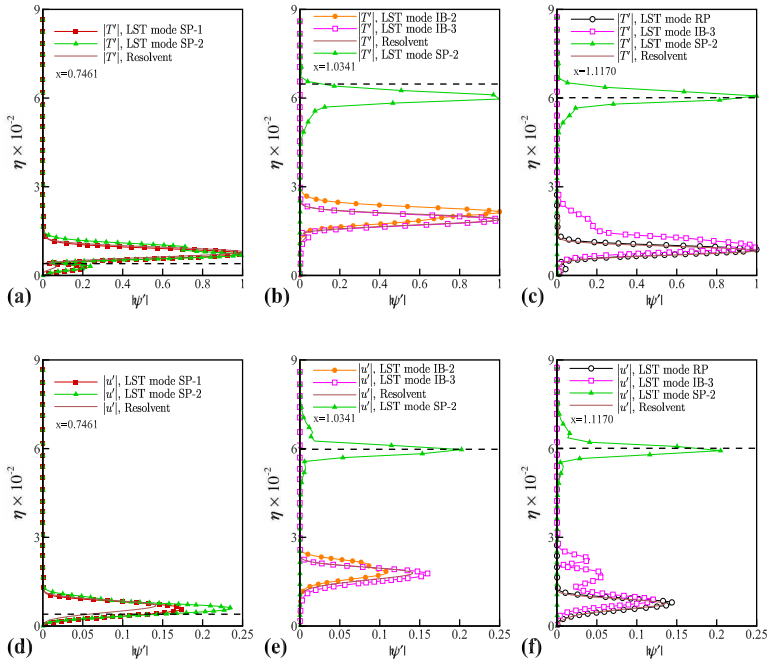

FIG. 16. Comparison of the disturbance shape for $\omega = 20$ and $\beta = 260$ between the resolvent response and the LST eigenfunction with AOA = -8°. The horizontal dashed line represents the location of the separation shock. All results are normalised by the maximum $|T'|$.

varies, confirming that they possess signature of Görtler instabilities. For instance, at AOA = -8° and AOA = $+8^\circ$, Fig. 15 shows the variation in the growth rates of modes SP-1 and SP-2 with curvature, respectively. The result is obtained by gradually changing the local curvature K from its actual value K_0 to zero in the LST operator. It can be observed that the growth rates are highly sensitive to the streamline curvature. When the curvature is artificially set to zero, all unstable modes disappear. These observations are consistent with the baseline AOA = 0° in our previous study[15], thereby demonstrating that the shear-layer modes at large positive or negative AOAs are still unsteady Görtler modes.

In summary, an enlarged separation bubble and abrupt change in streamline curvature may facilitate the emergence of new unstable modes. As the AOA decreases from AOA = 0° to AOA = -8°, the number of observed unstable modes increases from 8 to 13. These additional modes are closely associated with the discontinuous high-curvature regions shown in Fig. 2. In contrast, only 6 unstable modes are observed at AOA = $+8^\circ$. Moreover, the maximum growth rates of the modes exhibit a clear dependence on the AOA: they gradually increase as the AOA decreases to negative, and decrease as AOA increases to positive.

E. Comparison of shear layer modes between LST and Resolvent Analysis

It has been shown that the parallel-flow stability analysis remains applicable for shear-layer modes at AOA = 0°[15]. Currently, the applicability needs an examination at higher AOAs. For instance, the case AOA = $+8^\circ$ awaits an investigation, where widespread continuous high-curvature regions are present. It remains uncertain whether LST can accurately capture shear modes under such conditions. Therefore, we select two extreme cases, AOA = -8° and AOA = $+8^\circ$, and compare the perturbation shapes obtained via LST eigenfunctions with responses derived from resolvent analysis.

For AOA = -8°, Fig. 16 and Fig. 17 show the temperature and velocity perturbation profiles at three selected locations, with positions indicated in Fig. 18. In Fig. 16(a) ($|T'|$) and Fig. 16(d) ($|u'|$), the disturbance profiles are influenced by a combination of coexisting mode SP-1 and mode SP-2. Since SP-1 is dominant, the resolvent response of $|T'|$ and $|u'|$ more closely resembles that of SP-1. In Fig. 16(b) and Fig. 16(e), the disturbances are primarily governed by modes IB-2 and IB-3, with the resolvent response aligning more closely with the dominant mode IB-3. Furthermore, due to the influence

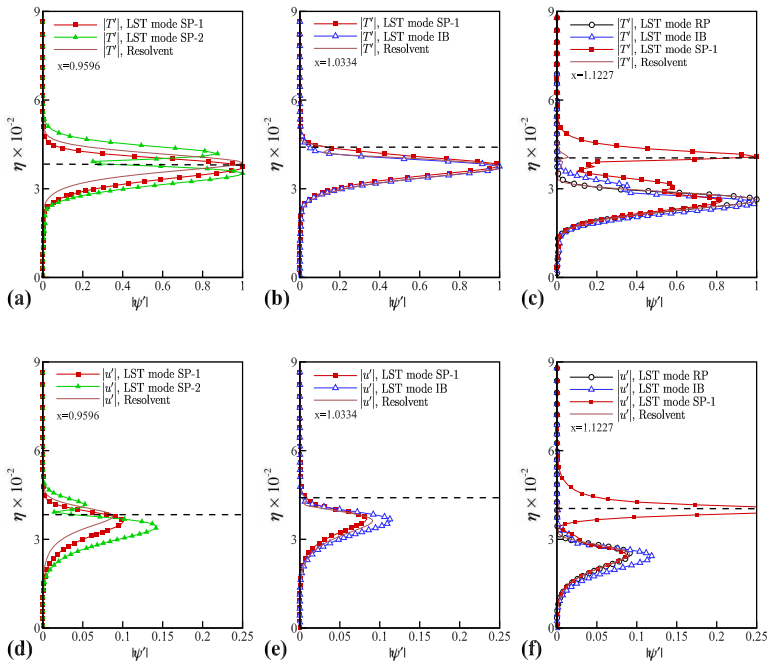

FIG. 17. Comparison of the disturbance shape for $\omega = 20$ and $\beta = 260$ between the resolvent response and the LST eigenfunction with AOA = $+8^\circ$. The horizontal dashed line represents the location of the separation shock. All results are normalised by the maximum $|T'|$.

of the separation shock, a peak associated with mode SP-2 is observed at the corresponding location. In Fig. 16(*c*) and Fig. 16(*f*), the peak of mode SP-2 consistently appears at the separation shock location. Since the growth rate of mode RP is significantly higher than those of IB-3 and SP-2 in this region, the influence of IB-3 and SP-2 on the disturbance structure is minimal, and the results from resolvent analysis show excellent agreement with mode RP obtained from LST. Combining the informative Fig. 13(*a*), it is suggested that if a dominant local mode exists, the global optimal response can be well approximated by its profile.

When the AOA increases to $+8^\circ$, as shown in Fig. 17(*a*) and Fig. 17(*d*), both the $|T'|$ and $|u'|$ profiles of SP-1 and SP-2 exhibit significant structural differences: SP-1 displays a single peak, while SP-2 exhibits two. Since at $x = 0.9596$ in Fig. 14(*e*), the growth rate of SP-1 is significantly higher than that of SP-2, the temperature and velocity perturbation profiles of the resolvent response align more closely with SP-1. In Fig. 17(*b*) and Fig. 17(*e*) at $x = 1.03$, the disturbance profiles are jointly influenced by mode SP-1 and mode IB. For $|T'|$, the eigenfunctions of SP-1 and IB are very similar. The overall resolvent response more closely matches mode IB. For $|u'|$, the perturbation profile aligns more closely with the eigenfunction of the dominant mode SP-1. Fig. 17(*c*) and Fig. 17(*f*) show several coexisting unstable modes of notable amplitude. For $|T'|$, both SP-1 and IB exhibit multiple peaks. The resolvent response agrees well with the eigenfunction of the dominant mode RP, though several smaller peaks also appear near the separation shock, suggesting influence from the less prominent mode SP-1. For $|u'|$, the resolvent response shows excellent agreement with mode RP, with a subtle peak at the separation shock corresponding to the peak location of SP-1.

In addition to comparing the eigenfunction shapes obtained from LST with the optimal response from resolvent analysis, it is also valuable to examine the differences in the growth rate between the two methods. The relationship between the N_0-factor from resolvent analysis and the growth rate is given by $\sigma = dN_0/dx$, from which the streamwise distribution of resolvent-derived growth rate is obtained and presented in Fig. 19. For AOA = -8° in Fig. 19(*a*), the LST-derived growth rate agrees well with the resolvent analysis result at $x = 1.1170$. However, a moderate discrepancy is observed at $x = 0.7461$, where the growth rate of mode SP-1 shows a relatively larger deviation from the resolvent result. A more pronounced discrepancy appears at $x = 1.0341$. This implies

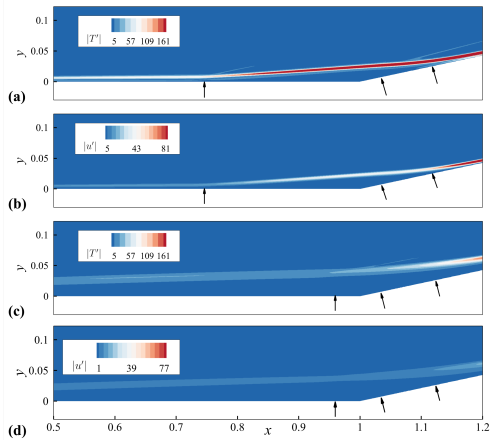

FIG. 18. Modulus of the optimal response with respect to temperature and velocity disturbances for $\omega = 20$ and $\beta = 260$, resulting from the unit-energy input in resolvent analysis. (*a*) and (*b*) correspond to AOA = $-8°$; (*c*) and (*d*) correspond to AOA = $+8°$. The arrows indicate positions at $x = 0.7461$, 1.0341 and 1.1170 (refer to Fig. 16) for AOA = $-8°$; and $x = 0.9596$, 1.0334 and 1.1227 (refer to Fig. 17) for AOA = $+8°$.

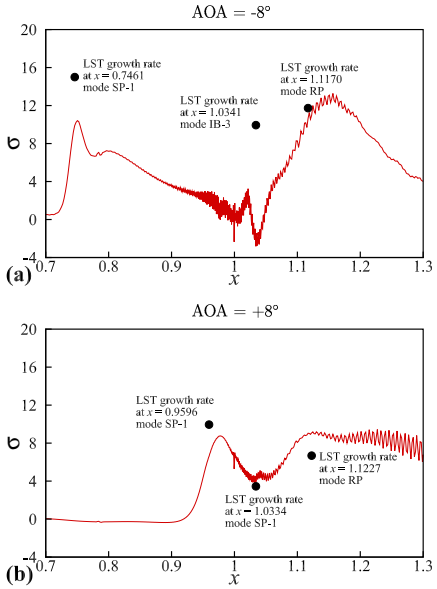

FIG. 19. Comparison of growth rates obtained from LST and resolvent analysis for $\omega = 20$ with $\beta = 260$ at (*a*) AOA = $-8°$ and (*b*) AOA = $+8°$. The black solid circles represent the dominant LST modes at the corresponding positions, while the red curves denote the growth rates derived from resolvent analysis.

that the short unstable region of mode IB-3 affects the global optimal response more in the mode shape (see Fig. 16(*b*) and Fig. 16(*e*)) than the local growth rate. For AOA = $+8°$, as shown in Fig. 19(*b*), the differences in the growth rate between the locally dominant LST modes and the resolvent analysis are relatively small. Considering the inherent non-parallel effects in high-curvature regions, these limited discrepancies remain within acceptable bounds, confirming that the dominant modes at AOA = $+8°$ maintain reasonable consistency with the resolvent analysis.

In summary, LST remains effective in predicting the growth of 3D low-frequency shear layers across various AOAs. At AOA = $-8°$, the LST-derived eigenfunctions generally show good agreement with the global optimal response, though localized discrepancies in growth rates are observed, with a notable deviation at $x = 0.7461$ and a more pronounced one at $x = 1.0314$. At AOA = $+8°$, the eigenfunctions maintain good agreement with the resolvent responses, while the growth rates exhibit reasonable consistency with the resolvent-derived values, despite the extensive high-curvature regions present on the upper surface of the separation bubble in Fig. 3(*h*).

V. CONCLUSION

In this paper, we investigate the effects of AOA on the flow stability of SWBLI, particularly focusing on high frequency 2D Mack modes and low frequency 3D shear layer instabilities. Altering the AOA significantly influences the morphology of the separation bubble. As the AOA is gradually reduced from zero, the separation bubble elongates and the shear layer extends. A more pronounced concave curvature emerges near the reattachment point at the rear portion of the bubble, and the upper surface near the leading edge becomes flatter. This results in a narrower high-curvature region on the top of the separation bubble, concentrating it mainly near the separation point and the rear concave portion of the bubble. Furthermore, as the AOA decreases, multiple individual narrow curvature zones gradually emerge within the concave region at the aft of the separation bubble. Conversely, an increase in AOA "compresses" the separation bubble, and its upper surface exhibits significant convex curvature. Consequently, the high-curvature region around the separation point and the central part of the bubble expands. The most abrupt streamline turning occurs near the separation point, where the curvature reaches its maximum.

LST and resolvent analysis were used to examine the influence of the separation bubble on the convective instability. For Mack modes, as AOA decreases, the separation zone is enlarged and LST results show that both the extent and growth rates of higher-order Mack modes are augmented. Conversely, as AOA increases, the separation zone shrinks and higher-

order unstable modes gradually vanish in the bubble. Moreover, the effect of streamline curvature in amplifying unstable modes is most pronounced at high positive AOAs. In particular, at AOA = $+8°$, an almost continuous band of instability forms across both high- and low-frequency ranges, similar to a broadband amplifier. The separation bubble generally exhibits selective amplification of low-frequency disturbances while appearing to "freeze" high-frequency perturbations. This behavior is especially evident when the separation bubble is elongated. However, at positive AOAs, the reduced extent of the separation zone may not provide sufficient physical space for full modal development, thereby weakening the freezing effect on high-frequency disturbances. As also observable in Fig. 9, the overall influence of the separation bubble on the flow field diminishes at high positive AOA.

Resolvent analysis reveals that as the AOA decreases from zero, the optimal gain region progressively expands toward higher spanwise wavenumbers. Conversely, under positive AOAs, the optimal gain overall narrows and shifts toward lower wavenumbers. As for the 3D low-frequency shear layer modes, these exhibit a clear dependence on streamline curvature, which is itself strongly influenced by the shape of the separation bubble. As depicted by Fig. 15, these shear layer modes are still unsteady Görtler modes at large positive or negative AOAs. Consistent with prior studies, multiple dominant unstable modes are observed at different streamwise locations. When AOA decreases, the growth rates of all modes increase, and new unstable modes emerge within the concave aft region of the separation bubble. In contrast, as AOA increases, the maximum growth rate decreases and fewer unstable modes are observed overall.

We also compare the shape of eigenfunctions obtained from LST with the resolvent responses at AOA = $-8°$ and AOA = $+8°$. In both of these extreme cases, the LST eigenfunctions and the resolvent responses show good agreement, indicating that the disturbance shape is primarily governed by the locally dominant unstable mode. However, marked discrepancies between LST and resolvent analysis in the local growth rate are observed for AOA = $-8°$, including a notable deviation for mode SP-1 near the separation point and a more pronounced discrepancy for mode IB-3 at $x = 1.0341$. Nevertheless, good agreement is found at $x = 1.1170$, and for AOA = $+8°$, the growth rates maintain reasonable consistency across all examined positions. These results collectively support the conclusion that LST remains applicable for the majority of SWBLI convective-instability studies.

The presented findings offer practical insights into the design and operation of hypersonic vehicles. Understanding how the AOA modulates instability amplification can inform transition prediction and control strategies on critical surfaces like scramjet intakes and control fins, where managing the boundary layer state is essential for aerodynamic performance and thermal protection. Future efforts may target the experimental validation of these instability mechanisms in ground-test facilities, as well as the extension of the analysis to more realistic three-dimensional components, such as swept wings or cone-flare configurations, in order to assess the robustness of the revealed physical mechanisms.

APPENDIX

The mode trajectory diagrams mentioned in the main text are provided below.

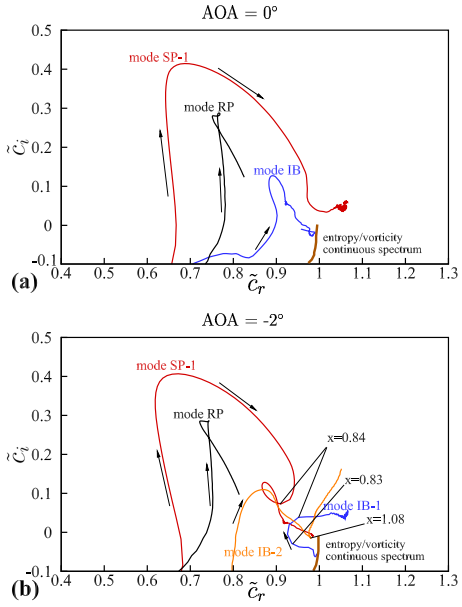

FIG. 20. Trajectories of modes in the complex plane: (*a*) corresponds to Fig. 13(*a*) and (*b*) corresponds to Fig. 13(*b*).

ACKNOWLEDGMENTS

This research is supported by the Start-up Fund for RAPs by the Hong Kong Polytechnic University (No. P0053712) and the Hong Kong Research Grants Council (No. 15203724). The resolvent analysis code provided by Prof. J. Hao is greatly appreciated.

DATA AVAILABILITY

The data that support the findings of this study are available from the corresponding author upon reasonable request.

AUTHOR DECLARATIONS

Conflict of Interest: The authors have no conflicts to disclose.

[1]K. Cassel, A. Ruban, and J. Walker, "An instability in supersonic boundary-layer flow over a compression ramp," Journal of Fluid Mechanics **300**, 265–285 (1995).
[2]P. Huerre and P. A. Monkewitz, "Local and global instabilities in spatially developing flows," Annual review of fluid mechanics **22**, 473–537 (1990).
[3]J. Chomaz, P. Huerre, and L. Redekopp, "Bifurcations to local and global modes in spatially developing flows," Physical review letters **60**, 25 (1988).
[4]M. Gaster, *The Structure and Behaviour of Laminar Separation Bubbles*, Reports and memoranda (H.M. Stationery Office, 1969).
[5]U. Rist and K. Augustin, "Control of laminar separation bubbles using instability waves," AIAA journal **44**, 2217–2223 (2006).
[6]C. S. Butler and S. J. Laurence, "Interaction of second-mode disturbances with an incipiently separated compression-corner flow," Journal of Fluid Mechanics **913**, R4 (2021).
[7]E. K. Benitez, M. P. Borg, P. Paredes, S. P. Schneider, and J. S. Jewell, "Measurements of an axisymmetric hypersonic shear-layer instability on a cone-cylinder-flare in quiet flow," Physical Review Fluids **8**, 083903 (2023).
[8]L. M. MACK, "Boundary-layer stability theory," in *Special Course on Stability and Transition of Laminar Flow*, AGARD Rep. 709, edited by R. Michel (AGARD, 1984) pp. 3.1–3.81.
[9]A. Fedorov, "Transition and stability of high-speed boundary layers," Annual review of fluid mechanics **43**, 79–95 (2011).
[10]P. Balakumar, H. Zhao, and H. Atkins, "Stability of hypersonic boundary layers over a compression corner," AIAA journal **43**, 760–767 (2005).
[11]K. M. Casper, S. J. Beresh, R. Wagnild, J. Henfling, R. Spillers, and B. Pruett, "Simultaneous pressure measurements and high-speed schlieren imaging of disturbances in a transitional hypersonic boundary layer," in *43rd AIAA Fluid Dynamics Conference* (2013) p. 2739.
[12]S. Laurence, A. Wagner, and K. Hannemann, "Schlieren-based techniques for investigating instability development and transition in a hypersonic boundary layer," Experiments in Fluids **55**, 1782 (2014).
[13]A. Pandey, K. M. Casper, D. R. Guildenbecher, S. J. Beresh, R. Bhakta, M. E. DeZetter, and R. Spillers, "Instability measurements in hypersonic flow on a three-dimensional cone-slice-ramp geometry," in *AIAA SciTech 2022 Forum* (2022) p. 1578.
[14]C. Butler and S. J. Laurence, "Interaction of hypersonic boundary-layer instability waves with axisymmetric compression and expansion corners," in *AIAA Aviation 2020 Forum* (2020) p. 3071.
[15]P. Guo, J. Hao, and C.-Y. Wen, "Understanding instability-wave selectivity of hypersonic compression ramp laminar flow," AIAA Journal **63**, 2580–2593 (2025).
[16]S. S. Diwan and O. Ramesh, "Relevance of local parallel theory to the linear stability of laminar separation bubbles," Journal of Fluid Mechanics **698**, 468–478 (2012).
[17]M. Karimi, "Compressibility effects on the Kelvin-Helmholtz instability and mixing layer flows," Doctoral disertation (2015), 10.21236/ada244320.
[18]A. Khraibut and S. Gai, "Bluntness and incidence effects in hypersonic flows with large separated regions," Journal of Fluid Mechanics **947**, A5 (2022).
[19]A. Roghelia, H. Olivier, I. Egorov, and P. Chuvakhov, "Experimental investigation of Görtler vortices in hypersonic ramp flows," Experiments in Fluids **58**, 139 (2017).
[20]J. Hao, S. Cao, P. Guo, and C.-Y. Wen, "Response of hypersonic compression corner flow to upstream disturbances," Journal of Fluid Mechanics **964**, A25 (2023).
[21]A. Sansica, N. D. Sandham, and Z. Hu, "Instability and low-frequency unsteadiness in a shock-induced laminar separation bubble," Journal of Fluid Mechanics **798**, 5–26 (2016).
[22]T. Jaroslawski, M. Forte, O. Vermeersch, E. Gowree, and J.-M. Moschetta, "Linear stability analysis on a laminar separation bubble subjected to freestream turbulence," in *14th ERCOFTAC SIG 33 Workshop, Progress in Flow Instability, Transition and Control* (2022).
[23]J. Ren and S. Fu, "Competition of the multiple Görtler modes in hypersonic boundary layer flows," Science China Physics, Mechanics & Astronomy **57**, 1178–1193 (2014).
[24]P. Guo, Z. Gao, C. Jiang, and C. Lee, "Linear stability analysis on the most unstable frequencies of supersonic flat-plate boundary layers," Computers & Fluids **197**, 104394 (2020).
[25]P. Guo, Z. Gao, C. Jiang, and C. Lee, "Sensitivity analysis on supersonic-boundary-layer stability subject to perturbation of flow parameters," Physics of Fluids **33**, 084111 (2021).
[26]P. Guo, F. Shi, Z. Gao, C. Jiang, C.-H. Lee, and C. Wen, "Heat transfer and behavior of the Reynolds stress in Mach 6 boundary layer transition induced by first-mode oblique waves," Physics of Fluids **34**, 104116 (2022).
[27]P. Guo, J. Hao, and C.-Y. Wen, "Interaction and breakdown induced by multiple optimal disturbances in hypersonic boundary layer," Journal of Fluid Mechanics **974**, A50 (2023).
[28]S. Cao, J. Hao, P. Guo, C.-Y. Wen, and I. Klioutchnikov, "Stability of hypersonic flow over a curved compression ramp," Journal of Fluid Mechanics **957**, A8 (2023).
[29]L. V. Rolandi, J. H. M. Ribeiro, C.-A. Yeh, and K. Taira, "An invitation to resolvent analysis," Theoretical and Computational Fluid Dynamics **38**, 603–639 (2024).
[30]B. Bugeat, J.-C. Chassaing, J.-C. Robinet, and P. Sagaut, "3D global optimal forcing and response of the supersonic boundary layer," Journal of Computational Physics **398**, 108888 (2019).
[31]Y. Wu, S. Yi, L. He, Z. Chen, and X. Wang, "Experimental investigations of supersonic flow over a compression ramp based on nanoparticle-tracer-based planar laser scattering technique," Experimental Techniques **40**, 651–660 (2016).
[32]J. Lu, H. Yang, Q. Zhang, X. Wen, and Z. Yin, "Experimental investigation of hypersonic laminar flow over a compression ramp," Journal of Fluids Engineering **144**, 021205 (2022).
[33]E. K. Benitez, S. Esquieu, J. S. Jewell, and S. P. Schneider, "Instability measurements on an axisymmetric separation bubble at Mach 6," in *AIAA Aviation 2020 Forum* (2020) p. 3072.
[34]X. Mao and H. M. Blackburn, "The structure of primary instability modes in the steady wake and separation bubble of a square cylinder," Physics of Fluids **26** (2014).
[35]J. Dähnert, C. Lyko, and D. Peitsch, "Transition mechanisms in laminar separated flow under simulated low pressure turbine aerofoil conditions," Journal of turbomachinery **135**, 011007 (2013).
[36]E. M. Eljack, "The structure and dynamics of the laminar separation bubble," Journal of Fluid Mechanics **998**, A56 (2024).